This paper appears in the IEEE Journal of Biomedical and Health Informatics, 2018.
DOI: 10.1109/JBHI.2017.2780192

Robotics-assisted Needle Steering around Anatomical Obstacles using Notched Steerable Needles

Mohsen Khadem, Carlos Rossa, Nawaid Usmani, Ron S. Sloboda, Mahdi Tavakoli

***Abstract*—Robotic-assisted needle steering can enhance the accuracy of needle-based interventions. Application of current needle steering techniques are restricted by the limited deflection curvature of needles. Here, a novel steerable needle with improved curvature is developed and used with an online motion planner to steer the needle along curved paths inside tissue. The needle is developed by carving series of small notches on the shaft of a standard needle. The notches decrease the needle flexural stiffness, allowing the needle to follow tightly curved paths with small radius of curvature (ROC). In this paper, first a finite element model of the notched needle deflection in tissue is presented. Next, the model is used to estimate the optimal location for the notches on needle's shaft for achieving a desired curvature. Finally, an ultrasound-guided motion planner for needle steering inside tissue is developed and used to demonstrate the capability of the notched needle in achieving high curvature and maneuvering around obstacles in tissue. We simulated a clinical scenario in brachytherapy, where the target is obstructed by the pubic bone and cannot be reached using regular needles. Experimental results show that the target can be reached using the notched needle with a mean accuracy of 1.2 mm. Thus, the proposed needle enables future research on needle steering toward deeper or more difficult-to-reach targets.**

***Index Terms*—Medical Robotics, Needle Steering, FEM Modelling, Motion Planning**

I. Introduction

Percutaneous needle insertions are used for diagnostic and therapeutic applications such as biopsy, drug delivery, and cancer treatment. The performance of needle-based interventions depends on accuracy of needle tip placement in target locations inside the tissue. Targeting errors are caused by human factors, imaging limitations, needle deflection, and needle/tissue reactions including soft tissue deformation, needle/tissue friction, and sliding of multilayered structures [1, 2]. In needle interventions, steerable flexible needles with asymmetric beveled tips are used to enhance control over needle deflection and reduce targeting error. A flexible needle with an asymmetric beveled tip has an uneven distribution of forces at the tip, which causes the needle to deflect from a straight path during the insertion. Using these needles, the surgeon can control tip deflection by axially rotating the needle and changing the orientation of the bevel tip. The beveled flexible needles have higher curvature compared to the stiff needles or needles with symmetric bevels. Using these needles surgeons can compensate for deviations caused by the aforementioned targeting error sources.

For needle insertions on a straight line, where the target lies on the needle insertion axis and the path is unobstructed, stiff needles are used and axial rotations are performed only to compensate for small deviations from the straight line. However, to reach divergent targets or targets obscured by obstacles, needles with high curvature or small radius of curvature (ROC) are needed [3]. Typically, researchers employ flexible nitinol wires instead of needles in their robotics-assisted needle steering strategies [4, 5, 6]. The nitinol wire is highly flexible and has a higher curvature in comparison with the clinically used stainless steel needles. A mean ROC of 190 mm is reported for nitinol-based needles tested in synthetic tissue [6, 7]. Okazawa *et al.* [8] proposed a precurved stylet that could be rotated and translated relative to a straight needle shaft to manually steer a needle in tissue. Webster *et al.* [9], and Sears and Dupont [10] extended the concept of telescopic pre-curved tubes to develop active concentric tubes. The concentric tube robots can be used to avoid critical structures and reach targets in human body. With appropriate pre-curvature selections and deployment sequences, concentric tubes are able to obtain high curvatures and provide a large design space of possible curves [11]. However, relatively large dimensions and high cost of manufacturing of concentric tube robots have limited application of concentric tubes in cost-efficient needle-based interventions.

Several researchers have developed tip-bent steerable needles to improve needle deflection curvature in tissue [12, 13]. The tip-bent needle consists of a flexible shaft with bent distal section. These needles can steer along highly curved paths as a result of the increased net lateral force acting at the bent distal end of the needle. Henken *et al.* developed an MRI steerable compatible needle with a manually controlled bent tip [12]. The outer diameter of the needle is 3.2 mm, which is relatively large compared to 1.3 mm 18G standard needles and can increase patient trauma. Swaney *et al.* [13] implemented a passive flexure in the bent tip of the needle to minimize the tissue damage while maintaining the increased maximum nominal curvature. van de Berg *et al.* [14] extended the idea of tip-bent needles to develop a tendon-actuated bent-tip steerable needle. Experimental studies testing bent-tip steerable needles have reported radii of curvature values from 51.4 mm to 176 mm [14, 15]. Adebar *et al.* [3] described the design of an articulated-tip steerable needle with outer diameter of 0.8 mm that allows payloads to pass through the needle.

To summarize, one can identify two main ways to increase the maneuverability of needles: 1) increasing needle flexibility,

This work was supported by the Natural Sciences and Engineering Research Council (NSERC) of Canada under grant CHRP 446520, the Canadian Institutes of Health Research (CIHR) under grant CPG 127768 and the Alberta Innovates - Health Solutions (AIHS) under grant CRIO 201201232.

M. Khadem (Corresponding Author), C. Rossa, and M. Tavakoli are with the Department of Electrical and Computer Engineering, University of Alberta, Edmonton, AB, T6G 2V4, Canada. {mohsen.khadem, rossa, mahdi.tavakoli}@ualberta.ca

R. S. Sloboda, and N. Usmani are with the Cross Cancer Institute and the Department of Oncology, University of Alberta, Edmonton, AB, T6G 1Z2, Canada. {ron.sloboda, nawaid.usmani}@albertahealthservices.ca

and 2) modifying needle design to increase needle/tissue interaction forces that bend the needle. Needle flexibility is improved by employing softer materials or thinner needles. Steering forces (i.e.,needle-tissue interaction forces that bend the needle) can be increased by decreasing the bevel tip angle, increasing the bevel surface, introducing a precurve near the tip, or a combination of the above [2]. Increasing needle/tissue interaction forces damages the tissue and consequently increases needle intervention's trauma [13]. Also, very thin or bent-tip needles are incapable of providing a working channel inside the needle.

A. Objective and Contribution

We modify commercially available disposable brachytherapy needles to develop a needle with improved deflection curvature and enhanced maneuverability. A novel notched needle is developed by carving small notches on a standard needle shaft as shown in Fig.1. By carving several consecutive notches on the needle shaft, the needle flexural strength and the needle's minimum achievable ROC are decreased. The width of the notches are smaller than the diameter of payloads. Thus, the needle provides a safe working channel for delivering payloads to target locations. An optimization algorithm is employed to optimize notch geometry and minimize needle ROC. A novel controller is developed and used to perform image-guided closed-loop needle steering experiments on a tissue phantom and demonstrate the feasibility of maneuvering around obstacles inside the tissue using the notched needle. The goal of the proposed research is not changing the current clinical setting or replacing the current needles with the proposed notched needles. We intend to provide another option in terms of needle selection so that surgeons can perform successful needle insertions in certain clinical scenarios where high needle deflection is required. A highly flexible needles can be used based on the requirements of the needle-based intervention. The idea of enhancing a surgical instruments flexibility by reducing its flexural rigidity via applying several external notches, has been proposed for several minimally invasive surgeries [16, 17]. This paper is divided into three main sections, namely, modeling, design, and controlled needle steering. In Section II, we develop a model of needle deflection inside soft-tissue using finite element method (FEM). Open-loop needle insertion experiments are performed in Section II-B to validate the model. In Section III, we describe the notched needle's design requirements and implement an optimization algorithm to estimate the optimal location of the notches on the needle shaft for achieving a desired curvature. Details of a novel motion planner used for obstacle avoidance in needle steering are presented in Section IV.

Validation of the notched steerable needle in achieving high curvatures in soft tissue and maneuvering around obstacles is presented in Section IV-D. We simulate a clinical scenario in prostate brachytherapy, where the target is obscured by pubic arch and standard needles can not reach it. Results demonstrate that the new needles can avoid an anatomical obstacle and reach the target. Results of the experiments are discussed in Section V.

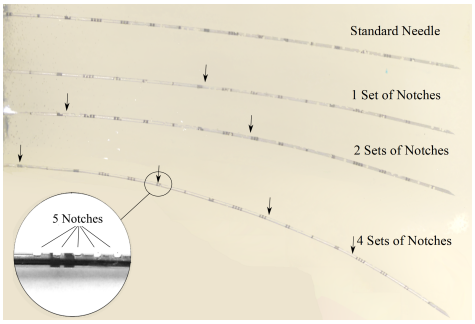

Fig. 1. A Comparison between deflection of a standard 18G brachytherapy needle and notched needles. Representative experimental needle insertion results for 140 mm insertion of needles with 0, 1, 2, and 4 sets of notches in plastisol tissue phantom are presented. Arrows show location of notches on the needle shaft.

II. Modeling

Here we use the finite element method (FEM) to develop a 2D model of the notched needle. The FEM model presented in this section was partially presented at the 2016 International Conference of IEEE International Conference on Advanced Intelligent Mechatronics (AIM), Banff, Canada, 2016 [18]. This section includes additional results and discussions. The needle is modeled as a beam with a non-constant cross section due to several notches made along the needle shaft. The modeling assumptions are: 1) The needle is torsionally stiff and the insertions and twists applied to the needle base are directly transmitted to the tip. 2) The needle has only 2-D planar deflection and the insertion plane is defined by initial orientation of the needle beveled tip. 3) The needle is modeled as homogeneous beam that is infinitely stiff in shear. 4) The axis of the prismatic beam is incompressible and needle shortening due to axial compression is neglected. However, axial forces can affect needle bending dynamics when the deflection is large.

The needle/tissue interaction forces including the tissue cutting force F_c, tissue deformation force F_s, and needle/tissue friction F_f are modeled as external excitation forces (see Fig. 4(a)). It is assumed that the needle is comprised of two parts. First part of the needle is outside the tissue, confined by the grid template. The template is used for guiding and positioning the needle during the insertion. The second part of the needle is inside the tissue. We employ a modified Euler-Bernoulli hypothesis to model the section of the needle that is inside the tissue as a clamped-free beam [18]. To model large needle deflections, we use a modified Euler-Bernoulli beam theory that considers the effects of large rotation of the needle elements and needle shortening along the insertion axis. In the following, we briefly introduce the 2D FEM model of the needle.

A. FEM model

Using the modelling approach presented in our previous work [19], the equations governing large deflection bending of the needle is

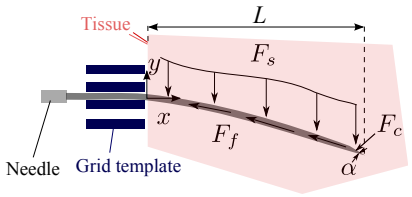

Fig. 2. A schematic of needle inside the tissue. The global coordinate system is fixed to the template. F_s, F_c, and F_f are the tissue deformation force, tissue cutting force, and friction along the needle shaft, respectively,α is the needle bevel angle and L is the length of the needle inside the tissue.

$$
\begin{aligned}
&-\frac{d}{dx}\left\{EA[\frac{du}{dx}+\frac{1}{2}(\frac{d\omega}{dx})^2]\right\}-f=0\\
&\frac{d^2}{dx^2}(EI\frac{d^2\omega}{dx^2})-\frac{d}{dx}\left\{EA\frac{d\omega}{dx}[\frac{du}{dx}+\frac{1}{2}(\frac{d\omega}{dx})^2]\right\}-q=0
\end{aligned}
\tag{1}
$$

ω and u are the longitudinal displacement and the transverse deflection, respectively, E is the modulus of elasticity, I is the second moment of inertia of needle cross section, and A is the needle cross section area. f and q are the distributed axial and transverse loads given by

$$
\begin{aligned}
f &= F_f + F_{cx}\delta(x-L)\\
q &= F_s + F_{cy}\delta(x-L)
\end{aligned}
\tag{2}
$$

where F_s and F_f are the tissue deformation force and friction along the needle shaft (measured per unit length). $F_{cx} = F_c\sin(\alpha)$ and $F_{cy} = F_c\cos(\alpha)$ are the axial and transverse components of tissue cutting force, respectively, and α is the needle tip's bevel angle. F_c is the total cutting force defined as the normal force applied to the needle beveled tip as it cuts through the tissue (see Fig. 4(a)). $\delta(\cdot)$ is the Dirac delta function. $L = \ell - x$ is the length of the needle inserted in the tissue and ℓ is the total length of the needle.

To calculate the needle/tissue interaction forces, we implement the models we developed in our previous work [20, 21]. Friction can be estimated as a function of insertion velocity per needle length using

$$F_f = \mu_c \text{sgn}(V) + \mu_v V \tag{3}$$

where μ_c and μ_v are the Coulomb and viscous friction coefficients, respectively, and V is the insertion velocity. Also the cutting force applied to the needle tip depends on the tissue viscoelastic stiffness modulus, the tissue pure elastic stiffness, needle bevel angle, and insertion velocity [21]. It can be assumed constant for a specific tissue and a given insertion velocity. To model the tissue reaction forces we implement the *time-delayed* tissue model presented by the authors in [19]. In the model, the magnitude of tissue deformation during the needle insertion is estimated as the difference between the cutting path (i.e., the needle tip trajectory across time) and the needle shape. Under this assumption, the distributed tissue reaction force is given by

$$F_s = E_S[\omega(x,t) - \omega(L, t-\tau)] \tag{4}$$

where E_S is the tissue stiffness, $\tau = \frac{\ell - L}{V}$, and V is the insertion velocity. F_s in (4), depends on both tissue properties and the amount of needle deflection. See [19] for more details.

TABLE I
EXPERIMENTALLY IDENTIFIED PARAMETERS AND CONSTANT KNOWN PARAMETERS OF THE FEM MODEL

Identified Parameters		
E_S [N/m^2]	F_c [N^2]	F_f [N/m]
1.190×10^5	0.963	4.208
Known Parameters		
E [GPa]	ℓ [m]	α [°]
200	0.2	20
I [m^4]		A [m^2]
Un-notched 7.75×10^{-14}		Un-notched 4.81×10^{-7}
Notched 6.8×10^{-14}		Notched 2.40×10^{-7}

Now following the FEM approach presented in [18] we can obtain the final FEM model of the needle deflection as

$$K(\Delta)\Delta = F(\Delta) \tag{5}$$

where K is the stiffness matrix and is a function of displacement of nodes Δ. F is the vector of nodal forces, which includes all needle tissue interaction forces and internal beam force/moments. The FEM problem given by (5) is nonlinear and should be solved iteratively. To solve the FEM problem, the Newton's iteration procedure is used [22].

In our *quasi-static* simulations, first we divide the total insertion depth into several small insertion steps, d_s. The simulation begins at the onset of insertion, needle initial length L is equal to d_s, with zero needle deflection, zero tissue reaction force, and only the cutting force applied to the needle tip. In the next step, $L = 2d_s$. We use the resulting needle tip deflection from the previous step and the model (4) to estimate the current tissue reaction force along the needle length. Estimated forces are implemented in the FEM model as nodal forces and the needle deflection is calculated. This approach is continued until the needle reaches the final depth.

We can compute the strains and stresses in the notched needle by post-processing the FEM and estimate the factor of safety of the notched needle as a measure of the strength of the needle in withstanding the expected loads applied to the needle. The axial stress in the beam is given by $\sigma_{xx} = E\varepsilon_{xx}$, where ε_{xx} is the summation of extensional and bending components of strain given by

$$\varepsilon_{xx} = \left[\frac{du}{dx} + \frac{1}{2}\left(\frac{dw}{dx}\right)^2\right] - y\frac{d^2\omega}{dx^2} \tag{6}$$

The factor of safety can be obtained by:

$$FS = \frac{\sigma_{TS}}{\sigma_{max}} \tag{7}$$

σ_{max} is the maximum stress in the needle, and σ_{TS} is the material ultimate tensile strength.

B. Results

In this section, needle insertion experiments are performed using the setup shown in Fig. 3 to verify the proposed FEM model and evaluate notched needle performance in achieving high deflection curvatures. In order to identify the tissue cutting force, the tissue stiffness per unit length of the needle and the friction force per unit length of the needle, we follow the

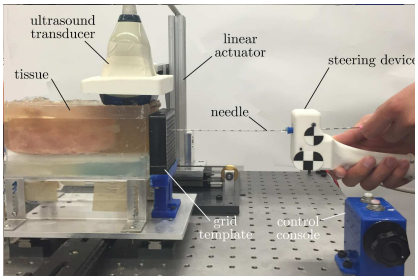

(a) Needle steering setup

(b) Template for carving the notches

Fig. 3. (a) The needle steering assistant used to perform needle insertion experiments [23]. The device can be used to automatically rotates the needle axially during the needle insertion. The probe of the ultrasound machine (SonixTouch, Ultrasonix, BC, Canada) is automatically moved to follow the hand-held device and provide images of the needle tip. The phantom tissue used in the experiments is made of 80% liquid plastic and 20% plastic softener (M-F Manufacturing Co., Fort Worth, TX, USA). The tissue's Young's modulus of elasticity is estimated to be 35 kPa using indentation tests. The elasticity of the synthetic tissues is similar to what is found in animal tissue [24]. (b) The 3D printed template used for carving notches on the needle.

approach discussed in our previous work [19, 21]. The values of the parameters of the needle steering model identified for constant insertion velocity of 5 mm/sec and known mechanical characteristics of the needle are given in Table I.

Results of needle deflection simulations using the parameters given in Table I are presented in Fig. 4. The simulations are performed for needle deflection in free space under 0.05 N load and the needle insertion in soft tissue up to a depth of 140 mm without rotation and with rotation at the depth of 70 mm. Simulations are performed for a standard needle and a notched needle with 3 sets of notches. Based on the simulation results, the mean ROCs of the notched needle in and outside the tissue is 53% and 70% smaller than the standard needle both, respectively. The highest estimated stresses for both needles in free space are at the needle base and almost similar ($\sim$ 18 MPa). The maximum stress for notched needle in soft tissue is near the notch closest to the needle tip in insertion with rotation and is equal to 1.25 MPa. Considering that the maximum strength of a needle made out of stainless steel Grade 316 is 480 MPa, the safety factor of the proposed notched needle is 380. This is a relatively high safety factor and ensures the needle will not break during the insertion.

We compare model predictions with experimentally obtained needle deflection to validate the model. In the experiments, sets of 5 equidistant notches with depth 0.3 mm and width 0.4 mm are manually carved at different locations on the needle shaft. The distance between each consecutive notch in a single set is selected to be 1.5 mm. Needle insertions are performed with a standard 18G brachytherapy needle (Eckert & Ziegler BEBIG Inc., CT, USA) and 18G brachytherapy needles with 1, 2, and 4 sets of notches. A single set of notches is carved in the middle of the needle, double sets are carved at the lengths of 66 and 133 mm, and quadraple sets are placed at lengths of 40, 80, 120, and 160 mm. The procedure introduced in [25] is used to calculate needle deflection from the ultrasound images. To validate the FEM model, we perform simulations using the parameters given in Table I and compare the results with the experimentally obtained needle deflections. The results are shown in Fig. 5. In the experiments, 6 insertions were performed at a constant insertion velocity of 5 mm/sec for each needle type.

TABLE II
COMPARISON OF EXPERIMENTAL DATA AND MODEL PREDICTIONS.

Number of Notch Sets	ROC_{exp}	ROC_{model}	ROC_{error}	RMSE [mm]
0	616	583	5.3%	6.85
1	452	478	5.7%	3.01
2	367	340	7.3%	4.09
4	205	233	10%	7.64

Table II summarizes the experimental results. Experimental mean ROC, ROC_{exp}, model predictions mean ROC of the deflected needle, ROC_{model}, as well as the prediction error, ROC_{error}, and root mean squared error (RMSE) of predicting ROC during the needle insertion are reported. The needle ROC reported in here and commonly assumed to be constant in the literature is the needle ROC in the local frame of the needle tip. The needle trajectories seen in in Fig. 5 are from a point of view of a fixed inertial-frame. We note that the local tip frame and the global inertial frame coincide when the insertion velocity is constant and the needle is not rotated. Thus, the data for the needle insertions without rotation are used to identify the needle's ROC. Throughout this paper, the ROC is calculated by fitting a circle to the global needle deflection when the needle is not rotated using nonlinear least-square method [26].

We also performed some experiments involving 180° axial rotation of the needle. A notched needle with two sets notches is inserted to a total depth of 140 mm at a speed of 5 mm/s, while either a single rotation is performed at a depth of 80 mm, or double rotations are performed at depths of 30 and 80 mm. 10 needle insertions are performed for each scenario. The maximum error in predicting the tip position is 1.74 mm at a depth of 89 mm for insertion with double rotations.

The experimental results show that carving four sets of equally spaced notches on the needle shaft improves the needle deflection curvature by 67%. The FEM model is capable of predicting the needle curvature with an accuracy of of 89%. RMSE is calculated as $\sqrt{\frac{\sum_{k=1}^{n}(\hat{y}_k - y_k)^2}{n}}$ and is used as a measure of the differences between values predicted by the FEM model, $\hat{y}$, and values observed in the experiments, y, for n data points. The largest deviation in final tip deflection was observed for the needle with one set of notches (6%).

III. DESIGN

The FEM model presented in Section II accepts the notch geometry (e.g., notch depth, width, and the location of the notches on the needle shaft) as the initial parameters. In this section, the model is employed in an optimization algorithm to estimate the number of notches and the optimal geometry of the notches required to achieve the highest possible curvature (or lowest ROC), while maintaining a reasonable safety factor. We will use the particle swarm algorithm (PSO) to calculate

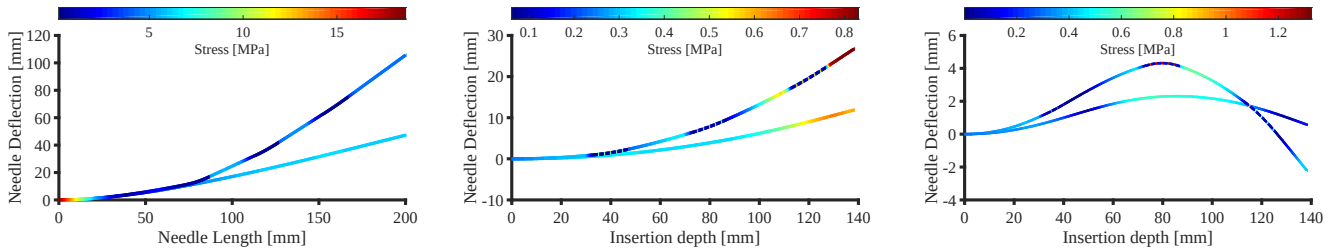

(a) Needle in free space (b) Needle in soft tissue (c) Needle in soft tissue with axial rotation

Fig. 4. Results of FEM model simulations. Simulations are performed for a standard needle and a notched needle with 3 sets of notches. The FEM model consists of 120 elements and the insertion is performed at 0.25 mm steps. A tolerance of 10^{-4} mm and a maximum allowable iteration number of 100 (per each insertion increment) are used in the FEM analysis and the iteration procedure. (a) Needle deflection in free space under 0.05 N load applied to the needle tip. (b) Needle insertion in soft tissue up to a depth of 140 mm without rotation. (c) Needle insertion in soft tissue up to a depth of 140 mm with rotation at the depth of 70 mm.

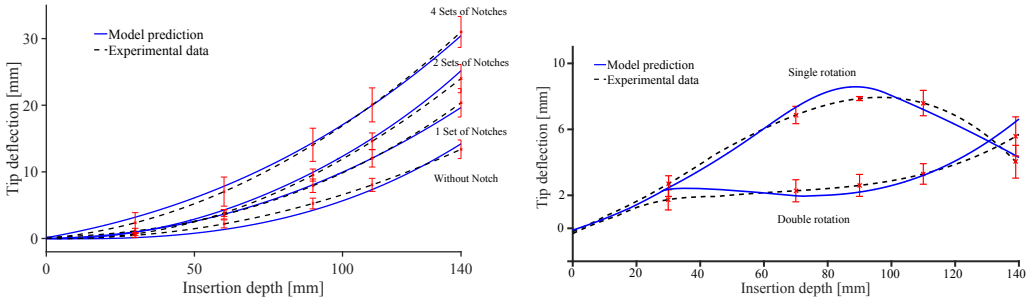

(a) Without axial rotation (b) With axial rotation

Fig. 5. A comparison of experimentally-obtained needle deflections and the corresponding model predictions for (a) needles with 0, 1, 2, and 4 set(s) of notches without rotation, and (b) needle with 2 sets of notches with single rotation at a depth of 80 mm and double rotations at depths of 30 and 80 mm. Error bars denote standard deviation.

optimal design soloution. PSO was first proposed by Kennedy and Eberhart [27] and has been proved to be useful on diverse engineering design applications such as structral shape optimization and topology optimization.In the following, we introduce the optimal problem for designing the notches and briefly discuss a modified PSO algorithm for solving the optimal problem.

A. Optimal Notch Design

The notched needle design involves carving several sets of notches on different locations on the needle shaft. Each set includes several consecutive notches. It is assumed the notch width and depth are both 0.5 mm. These design parameters are assumed constant to ensure the needle can provide a safe channel for delivering payloads with a diameter bigger than 0.5 mm. In the optimal design problem the number of sets of notches (N_s), the number of notches in each set (N_n), the distance between notches in each set (d_n), and each sets location on the needle shaft (d_s) are being optimized towards the minimization of the mean needle ROC during needle insertion to the depth of 140 mm. The number of sets and notches in each set are integers and varies between 1 and 10. To restricts the optimization to feasible solutions, constraints are imposed on the distance between the notches in each set [0.5, 5] mm and the notch sets' locations on the needle shaft [0, 200] mm. We also constrained the magnitude of safety factor to be above 250. The selected safety factor is conservatively selected high enough to consider the effects of mechanical failure, stress intensity factor and possibility of crack propagation around the notches, environmental effects, human factor and use error, and the consequences of engineering failure.

In total, the problem has variable dimensionality of 13 (maximum of 10 different notch set locations, the distance between notches, the number of notches, and the number of sets). The optimal problem can be programmed as a mixed integer constrained nonlinear optimization problem:

$$\begin{aligned} &\text{cost}(\overrightarrow{X}) = \min_{\overrightarrow{X}} \; ROC(\overrightarrow{X}) + \Lambda \frac{1}{FS(\overrightarrow{X})} \\ &\text{subject to} \quad A.\overrightarrow{X} \leq b \\ &\text{where } \overrightarrow{X} = (N_s, N_n, d_s, d_n), \\ &N_s, N_n \in \mathbb{N},\ d_n \in \mathbb{R},\ d_s \in \mathbb{R}^{10} \end{aligned} \tag{8}$$

A is a m-by-13 matrix, where m is the number of inequality constraints and b is a vector of length m. Λ is a weighting parameter that penalizes low safety factors.

The PSO makes use of velocity vector $\overrightarrow{V}$ to update the particles' position $\overrightarrow{X}$ in a swarm. Each particle corresponds to an initial solution of the optimal problem. The position of a particle i at iteration $k+1$ is updated by

$$\overrightarrow{X}^i_{k+1} = \overrightarrow{X}^i_k + \overrightarrow{V}^i_{k+1} \tag{9}$$

Velocity is updated based on the memory gained by each particle, as well as the knowledge gained by the swarm as a whole. Velocity for each particle is given by

$$\overrightarrow{V}^i_{k+1} = w\overrightarrow{V}^i_k + c_1 r_1(\overrightarrow{P}^i_k - \overrightarrow{X}^i_k) + c_2 r_2(\overrightarrow{P}^g_k - \overrightarrow{X}^g_k) \tag{10}$$

$\overrightarrow{V}_k^i$ is the velocity at iteration k, r_1 and r_2 represents random numbers between 0 and 1, $\overrightarrow{P}_k^i$ and $\overrightarrow{P}_k^g$ denote the best ever particle position and global best position up to iteration k, respectively. c_1 and c_2 are constants and vary between 0 and 1. w is the inertia weight. Based on the particle and velocity update rules and the optimal problem in (8), the algorithm is constructed.

Algorithm 1: Particle Swarm Optimization

```
Initialize all particles
  X_0^i = X_min + r(X_max − X_min),  V_0^i = 0, k = 0
while k < Max_iteration do
    for ∀X_k^i ∈ swarm do
        if A.X_k^i ≤ b then
            if cost(X^i) < cost(P^i) then
                P^i = X^i
            end
            if cost(X^i) < cost(P^g) then
                P^g = X^i
            end
        end
    end
    for ∀X_k^i ∈ swarm do
        V_{k+1}^i =
        wV_k^i + c1r1(P_k^i − X_k^i) + c2r2(P_k^g − X_k^g)
        X_{k+1}^i = X_k^i + V_{k+1}^i
        if A.X_{k+1}^i ≤ b then
            w = 0
            Go to 14
        end
    end
    k = k + 1
end
```

In Algorithm 1, three modifications are performed to satisfy the constraints:

1) All the design variables for each particle are randomly initialized to satisfy the lower and upper bounds imposed by the constraints.

2) In calculating $\overrightarrow{P}^i$ and $\overrightarrow{P}^g$, only the feasible particles that satisfy the constraints are counted.

3) The velocity vector of a particle that violates the constraints is restricted to a usable direction that will reduce the cost function while pointing backwards to feasible directions [28]. During the iterations, a new position for the violated constraint particles is defined by setting the inertia parameter w in (10) to zero. The new velocity is a weighted average of previous particles and points toward feasible regions of the design space. To update discrete design variables, a criterion known as the Nearest Vertex Approach (NVA) is used [28]. The NVA approximates the discrete-domain location to the nearest integer of the local discrete variable on the basis of the Euclidean distance. This method is used for the two aforementioned discrete variables, namely, the number of sets of notches (N_s) and the number of notches in each set (N_n).

TABLE III
OPTIMIZATION RESULTS INCLUDING NUMBER OF NOTCH SETS, NUMBER OF NOTCHES IN EACH SET, NOTCH LOCATIONS ON NEEDLE, MINIMUM ACHIEVABLE ROC, AND SAFETY FACTOR OF THE DESIGN.

N_s	N_n	d_n [mm]	d_s [mm]	ROC [mm]	FS
5	6	1.5	[88, 106, 153, 170, 190]	171	285

B. Optimization Results

Using Algorithm 1, the optimization is performed to estimate the optimal notch positions for achieving the maximum allowable deflection curvature. Both c_1 and c_2 in (10) are 0.5 and the inertia weight w is initially equal to 0.1. The number of particles in the swarm is 20 and the maximum number of iterations is 120. Λ is 0.11 and selected in an iterative trial and error process. We performed several optimization with different values of between 0.5 to 0.05 and we were able to get the minimum ROC for =0.11, while maintaining ta safety factor bigger than 280.

Optimization results after 100 iterations including the global best ROC, number of sets, number of notches in each set, the centers of the notch locations on the needle shaft, and the width of the notches are reported in Table. III. The estimated safety factor of the optimal solution is 285. We will use this needle in the following section to perform controlled needle steering with obstacle avoidance.

IV. Steering and Obstacle Avoidance

In this section, we introduce an online motion planner used for ultrasound-guided needle steering. Using the planner, several controlled experimental needle insertions are performed to validate the efficiency of the notched needles in manoeuvring obstacles.

A. Problem Statement

Motion planning for high DOF robots such as the needle steering system with infinite dimensionality is challenging, as the set of feasible configurations that guide the needle toward target lie in a small subspace of the whole configuration space. Here, we present a motion planning algorithm capable of steering the needle toward a desired target in real-time. We decompose the problem of motion planning into pre-planning and online motion-planning.

For pre-planning, we use a sampling based approach to generate a Probabilistic Roadmap (PRM) [29]. Sampling-based planners are an effective tool for high DOF motion planning. In PRM, a workspace to configuration space mapping is generated offline by associating a cell of the workspace to nodes in the configuration space. Given the inputs specified preoperatively (e.g., target and obstacle locations), PRM can be constructed by sampling from the configuration space of the robot, testing them for whether they are in the free space, target region, or obstacle collision space. PRMs are well suited as the roadmap can be precomputed offline, leading to an online cost of only performing a graph search. In the proposed approach, the computationally expensive PRM generation is done offline once before needle steering using the developed FEM model.

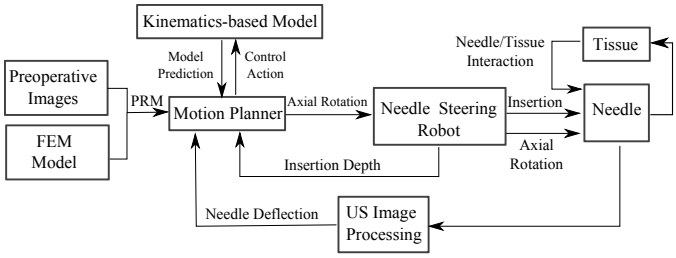

Fig. 6. Block diagram of the needle steering system.

For the online motion planning, a single query planner is used to search through the PRM with the sole goal of finding the final configuration that guides the needle to the desired target. The output of the online planner is a set of control inputs (i.e., appropriate rotation depths) during the needle insertion. The motion planner computes a large number of plans using the well-known kinematics based model of needle deflection [7] and selects a plan that guides the needle toward the desired target using the Rapid Random Tree (RRT) algorithm [30]. The output of the planner is the set of needle 180° rotation depth(s) that steers the needle to the target while avoiding obstacles. The kinematics-based model used in this paper assumes the needle moves on a path with a constant ROC. The only parameter of the model is the needle ROC [7] that is calculated in previous sections. The model has been widely used for image-guided needle steering in tissue [4, 5, 6].

The FEM is used for pre-planning as it is more accurate than the single-parameter kinematics-based model. The kinematics-based model is used for the online motion planning algorithm because the model is computationally efficient and the the planner needs to estimate needle tip deflection several times at high frequencies.

A schematic of the proposed needle steering scheme is shown Fig. 6. The setup shown in Fig. 3 is used to axially rotate the needle at appropriate depths during the insertion with the aim of minimizing targeting error while maneuvering the needle around anatomical obstacles. The experiments are done in a semi-autonomous manner, in which the surgeon is in charge of needle insertion to ensure the safety of the procedure, while the motion-planner is in charge of autonomous control of the needle trajectory via axial rotations of the needle. The needle insertion are performed by skilled a brachytherapist. The insertion velocity selected is in the range of clinical needle insertions. Clinical needle insertion velocities vary in between 5 to 50 mm/sec [31].

B. Motion Planner

To design the PRM, the needle steering problem is defined in the needle *configuration space*, $\mathcal{C}$. Assuming the needle moves in the 2D insertion plane, the needle *workspace* is a Euclidean space $\mathcal{W} = \mathbb{R}^2$. The configuration space, $\mathcal{C}$, is the space of possible control actions (i.e., depth(s) of needle rotation(s)), whose values identify the configuration of the needle tip in the workspace. The motion planning problem is: given an initial and a target position of the needle tip in $\mathcal{W}$, find (if it exists) a sequence of needle axial rotations that steers the needle between the initial and target positions while avoiding collisions with the obstacles. Considering symmetry of rotation depths (e.g., rotations at depths of 40 and 80 mm and rotations at 80 and 40 mm are equal) the configuration space is an n-dimensional simplex, where n is the number of rotations. For instance, if the maximum allowable number of rotations is 3, the configuration space forms a tetrahedron. Fig. 7 shows the workspace and Fig. 8(a) shows the configuration space for maximum of 3 rotations. The motion planner searches through the configuration space to find a sequence of rotation depths that steers the needle toward the target position while avoiding collisions. In order to solve the planning problem we decompose the configuration space into several disjoint cells. Assuming the distance between two consecutive rotations is at least 5 mm we can decompose $\mathcal{C}$ into several smaller simplices shown in Fig. 8(a).

In order to characterize paths that represent a solution in the configuration space – those that avoid collisions between needle tip and obstacles – it is necessary to build the image of the obstacles in the configuration space. Assuming the obstacles are closed, we define $\mathcal{C}_{obs}$ as the union of all subsets of the configuration space that cause a collision. To find the $\mathcal{C}_{obs}$ we estimate the needle trajectory using the FEM model at every vertex in the decomposed configuration space. The boundary of $\mathcal{C}_{obs}$ is the locus of configurations that put the needle in contact with an obstacle. Same approach can be used to find the goal region in configuration space. The goal region is defined as a set of rotation depth that will lead the needle tip to the proximity of the target while avoiding obstacles (see Fig. 8(b) and 8(c)). Now we can use the RRT algorithm to search the obstacle free space in $\mathcal{C}$ and find the optimal solution that steers the needle toward goal region. Description of the RRT motion planner algorithm is given in Algorithm 2.

Algorithm 2: Motion Planner

```
Initialize configuration space
C_free = C(N, D_0) − C_obs
while q_goal = ∅ ∧ t < T_max do
    q_rand = Rand_conf(C_free)
     q_near = Near_Vertex(q_rand, C_free)
     q_new = New_Conf(q_rand, q_near)
     path = Needle_model(q_new, ROC)
     T ← Add_Vertex(q_new)
    if path ∈ Goal then
        q_goal = q_new
    end
    Update T
end
```

The inputs of the RRT are the current depth D_0, the number of allowed rotations N, and the computation time available for planning T_{max}. The algorithm builds the free configuration space , $\mathcal{C}_{free}$, which is the subset of $\mathcal{C}$ that does not cause a collision. Then it generates a random candidate q_{rand} from the N-dimentional configuration space. Next, `Near_Vertex` runs through all the vertices (candidate rotation depths) in $\mathcal{C}_{free}$ to find the closest vertex to q_{rand}. `New_Conf` produces

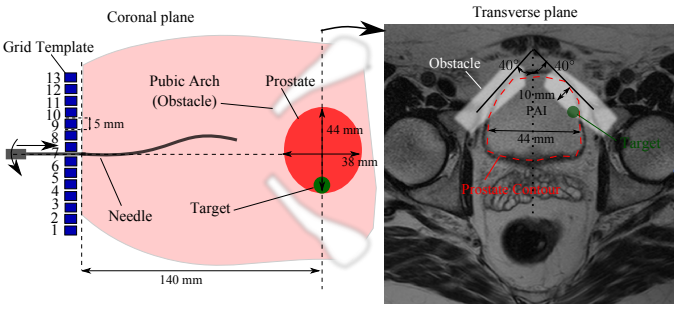

Fig. 7. Needle workspace in prostate brachytherapy in coronal and transverse plane. In brachytherapy the needle passing through a grid template is inserted in tissue, such that radioactive sources loaded in the needles can be placed near the tumor. The grid template has 13 holes placed 5 mm apart. In the transverse plane, the MR image with the narrowest pubic arch section is overlaid on that with the largest prostate contour in one patient. The image was obtained with the patient in the supine position. The angles of the right and left pubic arches are $40°$. The patient has 10 mm overlap of the pubic arch with the prostate margin.

a new candidate configuration q_{new} on the segment joining q_{near} to q_{rand} at a predefined arbitrary distance δ from q_{near}. The random tree $\mathcal{T}$ is expanded by incorporating q_{new} and the segment joining it to q_{near}. Next, needle tip path and targeting accuracy are obtained by inputting the selected rotation depths in the kinematics-based model of needle steering. When the needle path for the newly added configuration is found to lie in the target region ($Goal$), or when the computation times exceeds T_{max} the RRT planner terminates. Once the algorithm stops, the output q_{goal} contains the set of rotation depths that will bring the needle towards $Goal$ region. RRT expansion procedure results in a very efficient exploration of $\mathcal{C}$ and the procedure for generating new candidates in RRT is intrinsically biased toward regions of $\mathcal{C}$ that have not been visited.

The RRT has been used for needle steering in [4, 5].]text-colorredUnlike the approach presented here, RRT algorithm used in [4, 5] searches all the feasible needle trajectories toward a target, as obtained from a nonholonomic model of the needle. The algorithm then solves the inverse kinematics of the model to find the rotation inputs for following the selected trajectory. In contrast, our search space is constrained by the possible control inputs and the number and depths of rotations directly. Therefore, there is no need to solve for inverse kinematics of the model, which makes the optimization problem faster. The RRT algorithm is designed to efficiently search nonconvex, high-dimensional, meshed spaces by randomly building a space-filling tree [30]. This is the reason that the RRT is employey to search the configuration space for an optimal control action. As it is shown in Fig. 8(b) and 8(c) the free configuration space, $\mathcal{C}_{free}$, is a gridded, nonconvex, n-dimensional space.

C. Simulation Study

Two scenarios are used to validate the performance of the notched needle in enhancing targeting accuracy in needle steering.

1) The needle is steered on a straight line to reach a target placed at a depth of 140 mm.
2) The needle is steered to reach a target at the depth of 140 mm while avoiding the obstacle in the proximity of the target.

The 1st scenario is similar to conventional needle insertion in prostate brachytherapy, where the needle should be inserted along a straight line within the tissue. The 2nd scenario represents needle steering when there is a severe Pubic Arch Interference (PAI). PAI is common when the prostate volume is larger than 50 cm^3. PAI is also observed in the presence of a narrow pubic arch even in patients with a small prostate volume [32]. Brachytherapy is often not prescribed in case of PAI. PAI occurs in less than 10% of patients with early signs of prostate cancer [32]. Here, to validate the performance of the notched needles in obstacle avoidance we simulate a very severe case of PAI reported in the literature [32] (see Fig. 7).

In this scenario, there is a 10 mm interference between pubic arch and the prostate. The right and left angles to the inner border of the pubic rami are $40°$. The prostate is 44 mm in width, 31 mm in height, and 38 mm in length. The prostate dimentions are selected based on the average prostate size reported for men between the ages of 40 and 50 [33]. The 2 mm circular target is placed on one side of the prostate in a plane in the middle of the prostate that contains the largest prostate contour.

Results of the offline simulation of the motion planner with and without an obstacle are shown in Fig. 8. The goal is to steer the needle towards a target placed at a depth of 140 mm in the presence of PAI. In the simulations, the maximum allowable number of rotations is 3 and we used the FEM model of notched needle described in Section II to calculate the obstacle and the target region. We build the obstacle collision region ($\mathcal{C}_{obs}$) and the goal region through an exhaustive offline search. We estimate the needle trajectory using the FEM model at every node in the decomposed configuration space. In the simulations, the needle is inserted from grid point number 5 in the template (see Fig. 7). Based on the simulation results shown in Fig. 8(b) and Fig. 8(c), the obstacle region for both needles are almost the same. However, the target region for the notched needle is 215% larger than the standard needle target region, which indicates that the possibility of reaching to the target with the notched needle is more than the standard needle in the presence of PAI.

The number of possible control actions (i.e., sequence of rotation depths that steer the needle to the target) as a function of the insertion point (i.e., the grid number) for the two needles is shown in Fig. 8(d). The number of the possible control actions is significantly larger for the notched needle regardless of the insertion location. The best grid points for the notched needle and the standard needle are 8 and 7, respectively. We will use these grid points in the experiments.

D. Experimental Results

We executed the motion planner on an Intel Core i7 (2.93 GHz) PC at frequency of 30 Hz, which is equal to the US imaging frequency used to acquire the feedback for the motion planner (see Fig. 6). The planner generates a larger number of feasible motion plans, averaging over 300 plans at 30 Hz, over

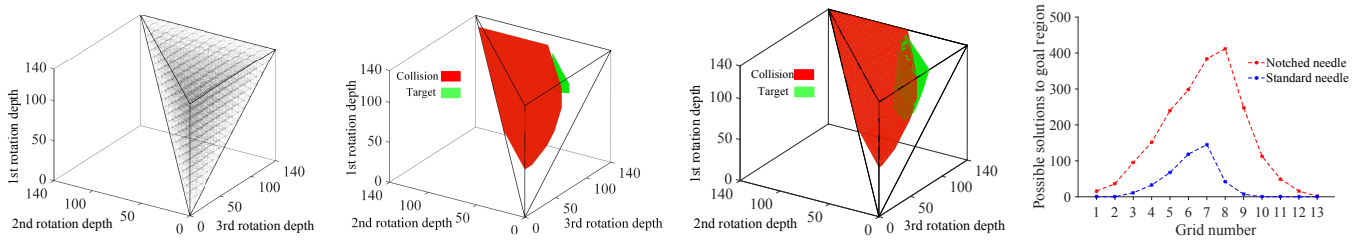

(a) Needle steering configuration space (b) Regions of goal and collision for standard needle (c) Regions of goal and collision for notched needle (d) Number of needle steering solutions vs. needle point of entry

Fig. 8. (a) Needle configuration space for a maximum of 3 axial rotations and a maximum insertion depth of 140 mm. (b) The configuration space for needle insertion from grid 5 with obstacle avoidance for the scenario shown in Fig. 7. The regions of obstacle collision and goal achievement are shown in red and green, respectively.(c) The configuration space for insertion of the notched needle from grid 5 with obstacle avoidance for the scenario shown in Fig. 7. (d) Comparison of offline path planning with the notched and standard needle. Number of possible solutions, i.e, sets of rotation that will steer the needle to the target while avoiding obstacles, are shown with respect to the selected template grid for insertion (see Fig. 7).

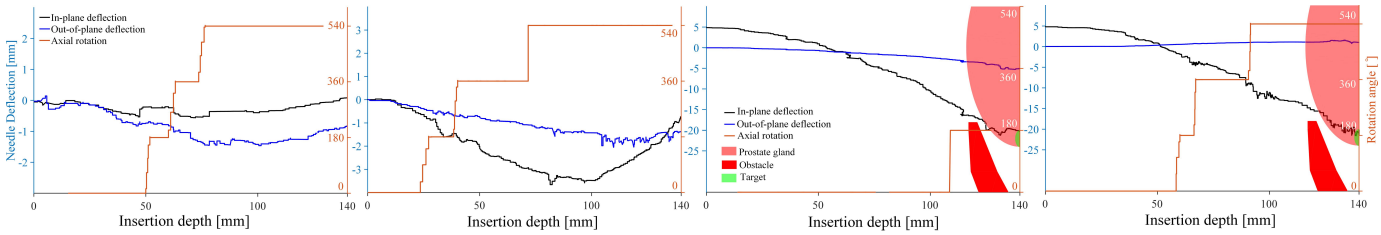

(a) Notched needle

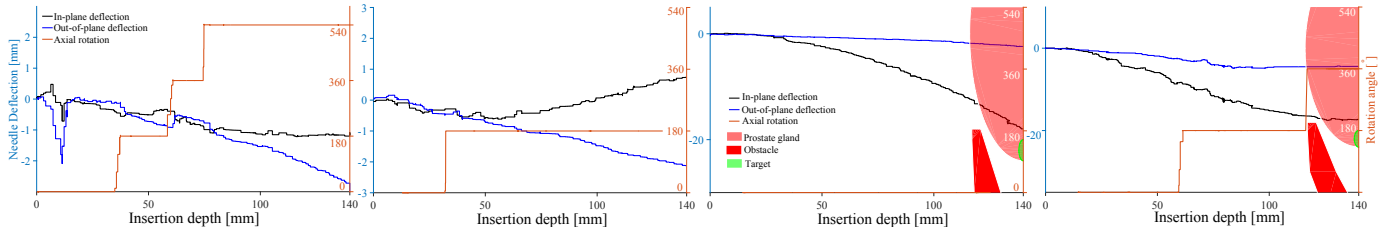

(b) Standard needle

Fig. 9. Representative experimental needle steering results for needle insertion on a straight line and needle insertion with obstacle avoidance for (a) notched needle, (b) standard 18G brachytherapy needle. Corresponding controller input command (i.e, needle axial rotation), needle out- of-plane deflection, and insertion velocity are shown in the figures.

which it selects the first plan that guides the needle toward the target. This number depends on many factors such as the current needle insertion depth, current needle deflection, desired targeting accuracy, and etc. Results of needle steering experiments for the notched needle designed in Section III and the standard 18G brachytherapy needle are shown in Fig. 9(a) and Fig. 9(b), respectively. In the experiments, the online motion planner is used to steer the needle. The planner uses the Kinematics-based model and the ROC for the needles are 583 and 171 mm, respectively (see Sections II-B and III-B). Experimental results for the two scenarios and the two needles are summarized in Table IV. The mean targeting error for 10 insertions e_{mean}, maximum targeting error e_{max}, and mean of out of plane deflection for 10 trials e_{out} are reported. The maximum targeting error for the notched needle in the first and second scenario are 1.21 mm and 1.85 mm, respectively. Also, the maximum out of plane deflection for the notched needle is 1.35 mm and occurs in the needle steering with obstacle avoidance.

TABLE IV
COMPARISON OF EXPERIMENTAL DATA AND MODEL PREDICTIONS.

	Notched needle		Standard needle	
	1st scenario	2nd scenario	1st scenario	2nd scenario
e_{max}	1.21	1.85	1.16	5.6
e_{mean}	0.90	1.26	0.85	4.1
e_{out}	0.62	1.35	1.05	1.67

V. DISCUSSION

The experimental validation results described in Sections II-B, II-B, and IV-D demonstrate that the notched needle is able to achieve higher deflection curvature in soft tissue than the standard needle (75% smaller ROC). We compared the performance of the designed notch needle with a standard brachytherapy needle in two different case studies. The first case intends to steer the needle on a straight line. The second case steers the needle toward a target partially obscured by an anatomical obstacle. Both needles showed the same performance for the first scenario. However, in the second scenario the motion planner mostly fails to steer the standard needle to the target in the presence of PAI (see Fig. 9(b)).

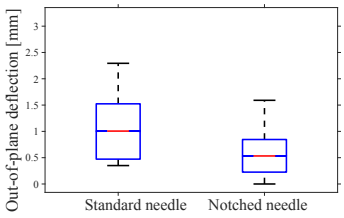

Fig. 10. A comparison between out-of-plane deflection of the notched needle and the standard needle. Experimental data for 10 trials are reported. Red line indicates median error, blue box indicates 25th and 75th percentile, and whiskers indicate minimum and maximum error.

40% of the insertions using the standard needle collides with the obstacle and the minimum targeting error when the needle passes the obstacle is 3.80 mm, which is 3 times more than the notched needle. Changing the point of entry can increase the needle insertion accuracy. We performed several other insertions from different grid points. 5 insertion trials were performed for each grid point. Changing the point of entry for the standard needles from 7 to 5,6, and 8 increased the possibility of collision. Results demonstrate that 47% of the insertions made from the grid points No. 5, 6, and 8 lead to collision, unlike the insertions from grid point 7 where no collision was detected. Thus, grid point 7 is more suitable for standard needles.

In most needle-based interventions such as prostate brachytherapy, the target is typically defined on a straight line starting at the entry point in tissue and up to a certain depth. The grid template placed outside the tissue is used to position the needle in a fixed insertion plane that contains the target. However, due to many factors such as needle/tissue reaction forces and tissue in-homogeneity the needles bend out of the deflection plane and reduce needle insertion accuracy. The designed notched needles tend to bend in one plane and have less out-of-plane deflection compared to the standard needles. Conventional needles have constant isotropic flexural strength. However, the designed notched needles have less flexural strength in the needle deflection plane and more strength in the plane normal to the needle deflection plane. The notches on the needle shaft reduce the overall needle's flexural strength defined as the needle's modulus of elasticity times second moment of inertia (EI). The notches are carved in a plane that is perpendicular to the deflection plane (i.e., normal to the bevel, see Fig. 1). Thus, the second moment of inertia in the deflection plane is smaller than the normal plane. For a notch with a depth of 5 mm, the needle flexural strength in the deflection plane in the proximity of the notch is less than a quarter (24%) of the flexural strength in the normal plane. Thus, the notched needle is more resistant to out-of-plane deflection and is disposed to bend in one plane. Fig. 10 shows the mean and the standard deviation of the out-of-plane deflection for the notched needle and the standard needle in needle insertion on a straight line for 10 trials. Based on the results, the notched needle shows less out-of-plane deflection compared to conventional needles.

In our FEM model it is assumed that the tissue is homogeneous. In our previous work [21], we developed several analytic models that accurately predict needle/tissue interaction forces in heterogeneous multilayer tissue. In future, we will implement our previously developed and validated needle/tissue interaction force models in in-homogeneous tissue in the FEM model, improving realism and performance and enabling future applications in motion planning in a in-homogeneous tissue. The developed FEM model is highly nonlinear and computationally inefficient for online application. However in future, we intend to investigate possible scenarios for simplifying the model for possible application in real-time needle steering. We also neglected the effects of target and obstacle motion during the needle insertion. Future efforts will focus on providing a more realistic testing scenario. Needle steering tests will be conducted on biological tissue with moving targets. In this case, motion of the target can be tracked in the ultrasound images or compensated in the control algorithm using a soft tissue model that predicts target displacements. A single query planner, i.e, RRT, is used in the motion planner to search through the configuration space and find the first solution that guides the needle to the desired target. The planner selects the first plan that satisfies the desired accuracy out of several feasible plans (see Fig. 8(d)). Detailed studies will be performed in future to accurately evaluate the sensitivity and performance of the proposed approach by comparing the results with other optimal controllers.

The notches are manually carved at different locations on the needle shaft using a hand-held milling machine and the 3D printed template shown in Fig. 3(b). Precautions were taken during carving the needles to make sure all the notches are the same size. In future, we will automate this process to ensure the notches are homogeneous and smooth, reducing the possibility of damaging the tissue. Also, the selected value of safety factor in the design process is high enough to ensure the safety of the design. However, there is a trade-off between needle integrity (measured via the safety factor) and the achievable radius of curvature (ROC). In future, optimal value of safety factor, which guarantees safety and allows to reach higher curvatures, will be calculated through rigorous testing based on standards for designing surgical needles.

In the design section, the notch width and depth are both fixed at 0.5 mm, which is smaller than the inner diameter of the needle. These design parameters are assumed constant to ensure the needle can provide a safe channel for delivering payloads with a diameter bigger than 0.5 mm, which is the case for radioactive seeds in prostate brachytherapy. However, there is a risk of leaking for delivering or preserving liquids. This can be avoided by coating the needles with super-elastic materials that does not increase needle rigidity but reduce the chance of leakage. Feasibility of silicone coating of surgical needles has been previously studied in the literature [34]. A soft coating also reduces the contact between the notches and the tissue, thus, eliminating the possibility of damaging the tissue. We intend to investigate the possibilities of coating the notched needles and other possible mitigating strategies for implementing the proposed needle in clinic in future work.

VI. Concluding Remarks

In this paper, we developed a new notched steerable needle that could follow tightly curved paths with high curvatures by

modifying commercially available disposable brachytherapy needles. The results demonstrate that our newly developed needles can achieve a minimum ROC of 171 mm, which is 75% less than a standard brachytherapy needle and very close to the ROCs of tip-articulated or wire-based needles reported in the literature [3, 7, 13]. Unlike the previous needles with improved curvature, the introduced notched needle provides a safe channel for delivering payloads to target locations. The ability of the notched steerable needle in achieving a high curvature is validated by performing several controlled needle insertion experiments on a tissue phantom. We also proposed an online motion planner for needle steering in soft tissue. The notched needle design combined with the closed-loop image-guided needle steering approach is used to insert the needle toward a designated target in soft tissue while avoiding obstacles. Results demonstrate that with the optimum design of the notches, we can perform successful needle insertions in certain scenarios that is currently inadmissible.

REFERENCES

[1] C. Rossa and M. Tavakoli, "Issues in closed-loop needle steering," *Control Engineering Practice*, vol. 62, pp. 55 – 69, 2017.

[2] N. van de Berg, D. van Gerwen, and *et al.*, "Design choices in needle steering: A review," *IEEE/ASME Transactions o Mechatronics*, vol. 20, no. 5, pp. 2172–2183, Oct. 2015.

[3] T. Adebar, J. Greer, and *et al.*, "Methods for improving the curvature of steerable needles in biological tissue," *IEEE Transactions on Biomedical Engineering*, vol. PP, no. 99, pp. 1–1, 2015.

[4] S. Patil, J. Burgner, and *et al.*, "Needle steering in 3D via rapid replanning," *IEEE Transactions on Robotics*, vol. 30, no. 4, pp. 853–864, Aug 2014.

[5] G. J. Vrooijink, M. Abayazid, S. Patil, R. Alterovitz, and S. Misra, "Needle path planning and steering in a three-dimensional non-static environment using two-dimensional ultrasound images," *The International Journal of Robotics Research*, vol. 33, no. 10, pp. 1361–1374, 2014.

[6] D. Minhas, J. Engh, and *et al.*, "Modeling of needle steering via duty-cycled spinning," in *29th Annual International Conference of the IEEE Engineering in Medicine and Biology Society (EMBS)*, Aug 2007, pp. 2756–2759.

[7] R. Webster, N. Cowan, and *et al.*, "Nonholonomic modeling of needle steering," in *Experimental Robotics IX*. Springer Berlin Heidelberg, 2006, vol. 21, pp. 35–44.

[8] S. Okazawa, R. Ebrahimi, J. Chuang, S. Salcudean, and R. Rohling, "Hand-held steerable needle device," *IEEE/ASME Transactions on Mechatronics*, vol. 10, no. 3, pp. 285–296, June 2005.

[9] R. Webster, J. Romano, and N. Cowan, "Mechanics of precurved-tube continuum robots," *IEEE Transactions on Robotics*, vol. 25, no. 1, pp. 67–78, Feb 2009.

[10] P. Sears and P. Dupont, "A steerable needle technology using curved concentric tubes," in *IEEE/RSJ International Conference on Intelligent Robots and Systems*, Oct 2006, pp. 2850–2856.

[11] H. Gilbert, J. Neimat, and R. Webster, "Concentric tube robots as steerable needles: Achieving follow-the-leader deployment," *IEEE Transactions on Robotics*, vol. 31, no. 2, pp. 246–258, April 2015.

[12] K. R. Henken, P. R. Seevinck, and *et al.*, "Manually controlled steerable needle for MRI-guided percutaneous interventions," *Medical & Biological Engineering & Computing*, pp. 1–10, 2016.

[13] P. Swaney, J. Burgner, , and *et al.*, "A flexure-based steerable needle: High curvature with reduced tissue damage," *IEEE Transactions on Biomedical Engineering*, vol. 60, no. 4, pp. 906–909, April 2013.

[14] N. J. van de Berg, J. Dankelman, and J. J. van den Dobbelsteen, "Design of an actively controlled steerable needle with tendon actuation and FBG-based shape sensing," *Medical Engineering & Physics*, vol. 37, no. 6, pp. 617 – 622, 2015.

[15] T. Adebar, A. Fletcher, and A. Okamura, "3-D ultrasound-guided robotic needle steering in biological tissue," *IEEE Transactions on Biomedical Engineering*, vol. 61, no. 12, pp. 2899–2910, Dec 2014.

[16] P. J. Swaney, P. A. York, and *et al.*, "Design, fabrication, and testing of a needle-sized wrist for surgical instruments," *Journal of Medical Devices*, vol. 11, no. 1, pp. 014 501–014 501–9, Dec. 2016.

[17] J. S. Kim, D. Y. Lee, , and *et al.*, "Toward a solution to the snapping problem in a concentric-tube continuum robot: Grooved tubes with anisotropy," in *2014 IEEE International Conference on Robotics and Automation (ICRA)*, 2014, pp. 5871–5876.

[18] M. Khadem, C. Rossa, and *et al.*, "Introducing notched flexible needles with increased deflection curvature in soft tissue," in *IEEE International Conference on Advanced Intelligent Mechatronics (AIM), Banff, Canada*, 2016, pp. 1186–1191.

[19] ——, "A two-body rigid/flexible model of needle steering dynamics in soft tissue," *IEEE/ASME Transactions on Mechatronics*, vol. 21, no. 5, pp. 2352–2364, Oct 2016.

[20] ——, "Ultrasound-guided model predictive control of needle steering in biological tissue," *Journal of Medical Robotics Research*, vol. 01, no. 01, p. 1640007, 2016.

[21] ——, "Mechanics of tissue cutting during needle insertion in biological tissue," *IEEE Robotics and Automation Letters*, vol. 1, no. 2, pp. 800–807, 2016.

[22] O. Zienkiewicz, R. Taylor, and D. Fox, *The Finite Element Method for Solid and Structural Mechanics*, seventh edition ed. Oxford: Butterworth-Heinemann, 2014.

[23] C. Rossa, N. Usmani, R. Sloboda, and M. Tavakoli, "A hand-held assistant for semiautomated percutaneous needle steering," *IEEE Transactions on Biomedical Engineering*, vol. 64, no. 3, pp. 637–648, 2017.

[24] A. Choi and Y. Zheng, "Estimation of Young's modulus and Poisson's ratio of soft tissue from indentation using two different-sized indentors: Finite element analysis of the finite deformation effect," *Medical and Biological Engineering and Computing*, vol. 43, no. 2, pp. 258–264,

2005.

[25] M. Waine, C. Rossa, , and *et al.*, "Needle tracking and deflection prediction for robot-assisted needle insertion using 2d ultrasound images," *Journal of Medical Robotics Research*, vol. 01, no. 01, p. 1640001, 2016.

[26] J. J. Moré, *The Levenberg-Marquardt algorithm: Implementation and theory*. Berlin, Heidelberg: Springer Berlin Heidelberg, 1978, pp. 105–116.

[27] R. Eberhart and J. Kennedy, "A new optimizer using particle swarm theory," in *Proceedings of the Sixth International Symposium on Micro Machine and Human Science, 1995*, 1995, pp. 39–43.

[28] S. Chowdhury, W. Tong, and *et al.*, "A mixed-discrete particle swarm optimization algorithm with explicit diversity-preservation," *Structural and Multidisciplinary Optimization*, vol. 47, no. 3, pp. 367–388, 2013.

[29] L. E. Kavraki, P. Svestka, J. C. Latombe, and M. H. Overmars, "Probabilistic roadmaps for path planning in high-dimensional configuration spaces," *IEEE Transactions on Robotics and Automation*, vol. 12, no. 4, pp. 566–580, 1996.

[30] S. M. LaValle and J. J. Kuffner, "Randomized kinodynamic planning," *The International Journal of Robotics Research*, vol. 20, no. 5, pp. 378–400, 2001.

[31] T. Podder, D. Clark, D. Fuller, J. Sherman, and *et.al.*, "Effects of velocity modulation during surgical needle insertion," in *27th Annual International Conference of the Engineering in Medicine and Biology Society, IEEE-EMBS*, 2005, pp. 5766–5770.

[32] J. Fukada, N. Shigematsu, , and *et al.*, "Predicting pubic arch interference in prostate brachytherapy on transrectal ultrasonography-computed tomography fusion images," *Journal of Radiation Research*, vol. 53, no. 5, pp. 753–759, 2012.

[33] S.-J. Zhang, H.-N. Qian, and *et al.*, "Relationship between age and prostate size," *Asian Journal of Andrology*, vol. 15, no. 1, pp. 116–120, 2012.

[34] W. McClung, S. Daniel, and *et al.*, "Enhancing needle durability by silicone coating of surgical needles," *The Journal of Emergency Medicine*, vol. 13, no. 4, pp. 515 – 518, 1995.